Check for updates

JGR Atmospheres

RESEARCH ARTICLE
10.1029/2020JD033840

Diffusivity and Solubility of H_2 in Ice Ih: Implications for the Behavior of H_2 in Polar Ice

John D. Patterson[1] and **Eric S. Saltzman**[1]

[1]Departments of Earth System Science and Chemistry, University of California, Irvine, Irvine, CA, USA

Key Points:

- The diffusivity and solubility of H_2 in ice Ih were measured at temperatures relevant to polar ice sheets (199–253 K)
- The implications of these measurements for the interpretation of firn air and ice core measurements of H_2 are assessed and discussed

Correspondence to:
J. D. Patterson,
jdpatter@uci.edu

Citation:
Patterson, J. D., & Saltzman, E. S. (2021). Diffusivity and solubility of H_2 in ice Ih: Implications for the behavior of H_2 in polar ice. *Journal of Geophysical Research: Atmospheres*, *126*, e2020JD033840. https://doi.org/10.1029/2020JD033840

Received 10 SEP 2020
Accepted 13 APR 2021

Abstract Reconstructions of paleoatmospheric H_2 using polar firn air and ice cores would lead to a better understanding of the H_2 biogeochemical cycle and how it is influenced by climate change and human activity. In this study, the permeability, diffusivity, and solubility of H_2 are determined experimentally in ice Ih at temperatures relevant to polar ice sheets (199–253 K). The experimental data are used in conjunction with simplified diffusion models to assess the implications for: (a) Diffusion of H_2 from pressurized closed bubbles to open pores in polar firn, (b) diffusive smoothing of H_2 gradients in the ice sheet, and (c) post-coring diffusive losses of H_2 from ice core samples. The results indicate that diffusive equilibrium between open and closed pores is likely achieved in the firn lock-in zone. Diffusive smoothing of atmospheric variations is significant and should be accounted for in atmospheric reconstructions on millennial time scales. Diffusive losses from a bubbly ice sample are sufficiently slow that samples may be meaningfully analyzed for H_2 after storage on the order of a year. These results suggest that the mobility of H_2 in ice should not preclude the reconstruction of paleoatmospheric H_2 from firn air and ice cores.

Plain Language Summary Documenting the variations in atmospheric H_2 is useful for understanding how H_2 cycles through the Earth system. The polar ice sheets contain an archive of ancient air that could be used to reconstruct the history of atmospheric H_2. Because of its small size, H_2 is more mobile in ice than other trace gases such as methane or carbon dioxide. In this work, we experimentally determine the rate of permeation of H_2 in ice and use the results to assess how the mobility of H_2 in polar ice affects the incorporation of atmospheric H_2 into the ice archive and the interpretation of ice core measurements.

1. Introduction

The polar ice sheets contain a unique archive of ancient air that can be used to reconstruct atmospheric composition on timescales from decades to hundreds of thousands of years. Reconstructing paleoatmospheric trace gas levels requires an understanding of how trace gases are incorporated into the ice sheet and how they evolve in time as a function of burial depth and temperature (e.g., Etheridge et al., 1996, 1998). Gas molecules with small kinetic diameters (<3.60 Å) are highly permeable in ice, and information about the solubility and diffusivity of such gases in ice is needed to develop physical models of gas transport in the ice sheet (Huber et al., 2006; Ikeda-Fukazawa et al., 2005; Patterson et al., 2020; Severinghaus & Battle, 2006). For example, firn air enrichments in Ne/N_2 and O_2/N_2 relative to atmospheric ratios have been observed as a consequence of bubble compression and diffusion into the open pores of the firn (Severinghaus & Battle, 2006). Bubble compression below close-off depths can lead to vertical migration of diffusive gases in the ice sheet (Ahn et al., 2008; Craig & Chou, 1982; Jean-Baptiste et al., 1993, 2001). Permeability of small gases can also lead to changes in trace gas composition during storage of ice core samples. Such changes have been observed for O_2/N_2 ratios, He, and H_2 (Bender et al., 1995; Bereiter et al., 2009; Haan, 1996; Jean-Baptiste et al, 1993, 2001; Severinghaus & Battle, 2006). Gas diffusion between bubbles and clathrates in the bubble-clathrate transition zone is also responsible for small scale variability in ice core CO_2 and O_2/N_2 measurements (Lüthi et al., 2010). These high-frequency variations are smoothed by diffusion deeper in the ice sheet.

This study is focused on the solubility and diffusivity of molecular hydrogen (H_2) in ice. H_2 is one of the most abundant trace gases in the atmosphere, with a global mean level of 530 ppb (Novelli et al., 1999). Atmospheric histories of H_2 from firn air and ice cores would provide insight into the biogeochemical cycle

© 2021. American Geophysical Union. All Rights Reserved.

of H_2 and its relationship to climate and human activities. Firn air H_2 records from Greenland and Antarctica show significant changes in atmospheric H_2 over the past century (Patterson et al., 2020; Petrenko et al., 2013). Quantitative information about the mobility of H_2 in ice is required in order to interpret firn air and ice core records (Patterson et al., 2020).

Relatively little work has been published on the physical properties of H_2 in ice. The solubility of H_2 in ice near the melting point has been measured over a wide pressure range (Ildyakov & Manakov, 2014; Manakov et al., 2017; Namiot & Gorodetskaya, 1969). No measurements have been made at the lower temperatures relevant to polar ice core sites. Strauss et al. (1994) published an estimate of the diffusivity of H_2 in D_2O ice at temperatures of 25–60 K. Here, we conduct laboratory measurements of the permeability of H_2 in synthetic polycrystalline ice Ih over a wide temperature range (199–253 K) and analyze the data to estimate H_2 solubility and diffusivity. Implications of the results are discussed in terms of (a) H_2 behavior in firn air, (b) H_2 mobility with depth in the ice sheet, and (c) sampling/storage of ice core samples for H_2 analysis.

2. Experimental

2.1. Experimental Method

This study was carried out using a "block degassing" method. This involves exposing a block of ice ($1.5 \times 1.5 \times 0.5$ cm) to a pure H_2 atmosphere for several hours, (referred to as "charging") then replacing the H_2 with air and monitoring the H_2 outgassing as a function of time. This is similar in principle to methods used in prior studies of gas diffusion in ice (e.g., Noguchi et al., 2019; Satoh et al., 1996). In those studies, outgassing was carried out in a sealed evacuated chamber and quantified by monitoring the change in total cell pressure. Here outgassing was carried out in a flow of Ultra-zero air at a pressure of 1 atm and quantified by measuring the air flow rate and mole fraction of H_2 in the air exiting the diffusion chamber.

Experiments were carried out over a range of temperatures maintained to $<\pm 0.05$ K using three configurations. Experiments at 199.2–204.2 K were carried out in a temperature-controlled polystyrene foam box placed inside an outer insulated box containing dry ice. The polystyrene foam box contained an air-circulating fan, thermistor, and heater, with temperature control provided by a thermistor signal amplifier and Newport process controller. Experiments at 227.2 K were carried out in a low temperature freezer with digital temperature control (Scientemp Corp.). Experiments at 252.7 K were carried out in the temperature-controlled box placed inside a 249 K walk-in freezer. In this configuration, eutectic ice packs were placed in the polystyrene foam box to prevent temperature drift during defrost cycles.

The ice block is placed in a stainless steel "charging" chamber made from a KF-25 nipple sealed with Viton O-rings. Once the chamber and ice thermally equilibrate at the experimental temperature, a flow of pure H_2 is maintained for 12–72 h (5 mL min^{-1} STP; $P = 1$ atm). Subsequently, the sample is manually transferred to a second stainless steel "outgassing" chamber, sealed by Conflat flanges with copper gaskets (Figure 2). The second chamber is never exposed to pure H_2 to avoid outgassing of H_2 from chamber walls. A stainless steel cylinder was placed in the outgassing chamber to minimize dead volume. A mass flow controller regulates a flow of Ultra-zero air into the temperature-controlled box through a coil of copper tubing, and into the outgassing chamber (10 mL min^{-1} STP; $P = 1$ atm). The outflow from the outgassing chamber is routed to the GC/HePDD injection loop and analyzed for H_2 every 12 min. All tubing is 1/8" copper. The experiment is terminated when the H_2 levels in the air flow approach the limit of detection of the analytical system, about 24 h depending on ice sample size and H_2 exposure time.

During both the charging and outgassing phases of the experiment, the gas flows are pre-equilibrated with the experimental temperature by passage through a 2 m coil of copper tubing prior to reaching the chamber. For experiments carried out at 253 K, the Ultra-zero air flow was pre-saturated with water vapor prior to entering the outgassing chamber. This was done to minimize mass loss of the ice block to sublimation which would otherwise have been about 1% over 24 h. The pre-saturation chamber consisted of a stainless steel KF-25 nipple sealed with Viton O-rings that contained a similarly prepared block of

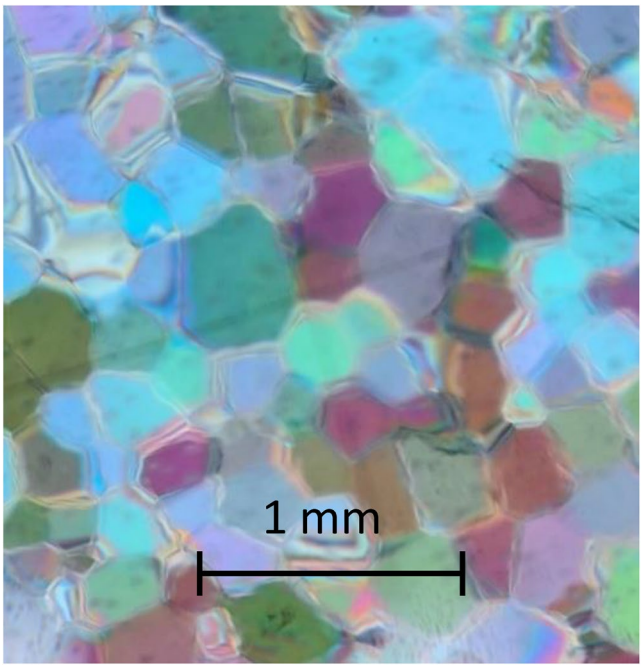

Figure 1. A piece of ice prepared as described in Section 2.1 imaged under a cross-polar microscope. This piece was thinned to about 0.5 mm for imaging.

ice. The pre-saturation chamber and ice was never exposed to pure H_2. The pre-saturation chamber was not required for experiments at colder temperatures.

Care was taken to avoid air inclusions during the preparation of the ice. First, a ¼" sheet of copper was precooled to −47°C and ultra-pure Milli-Q water was degassed by boiling for 15 min. At room temperature, a square nylon tube with 0.3 cm thick walls, a 1.5 × 1.5 cm inner cross section, and ~4 cm length is placed on the cold copper. 6 mL of hot water is pipetted into the square tube, and the water freezes from the bottom, excluding any remaining dissolved gas into the liquid above. After ~10 min, the remaining liquid water is poured off the top of the tube, and the ice is pressed out of the tube by hand. The top of the ice is then melted back to the desired thickness and simultaneously blotted with a Kimwipe to remove meltwater. The samples used in this study were typically 0.5 cm in thickness. The ice appears bubble-free under magnifications that reveal bubbles with diameters greater than 10 μm. While the presence of smaller bubbles cannot be ruled out completely, we estimate that undetected bubbles could bias the measured diffusivity and solubility high by not more than 5%–10%. Examination of a thinner (~0.5 mm) similarly prepared ice sample under a cross polar microscope revealed polycrystalline ice with a typical crystal size of ~0.3 mm (Figure 1). The c-axes of the crystals are randomly oriented.

2.2. Data Analysis

There are no published analytical solutions for diffusion from a rectangular block of finite dimensions. To analyze the experimental results, we used a 3-dimensional time-dependent finite-difference diffusion model. The model domain is the entire block of ice. A model grid is constructed with the unique length, width, and height of the ice blocks used in each experiment (L, W, and H). Non-uniform grid spacing is used to provide high resolution at the edges of the box where the strongest concentration gradients are present while minimizing computational costs. In the center of the model domain ($x = L/2, y = W/2, z = H/2$) normalized

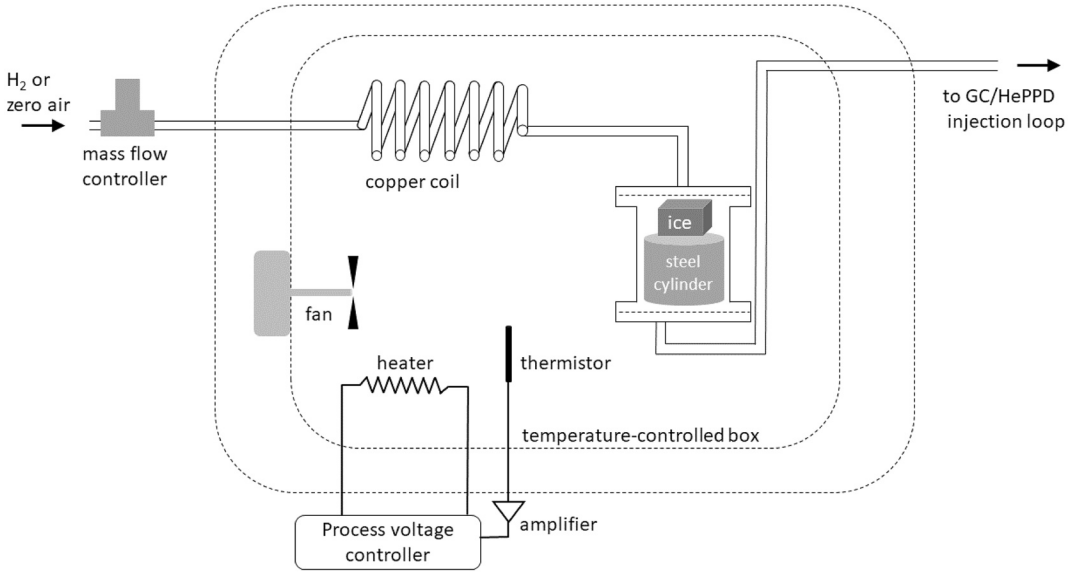

Figure 2. Schematic of the laboratory setup used to measure H_2 permeation in ice.

spacing (i.e., $\Delta x/L$) is 0.0385, 0.0385, and 0.0714 in the x, y, and z dimensions. Normalized grid spacing decreases linearly to 0.0015, 0.0015, and 0.0055 at the outer boundaries (i.e., $x = 0$, $x = L$). The governing equation for the model is Fick's second law:

$$\frac{\partial C}{\partial t} = D\nabla^2 C \tag{1}$$

where C (mol m^{-3}) is the concentration of H_2 in the ice and D (m^2 s^{-1}) is the diffusivity constant of H_2 in ice. A Dirichlet boundary condition is imposed where the concentration in the boxes at the edge of the domain is prescribed. During the charging period, the concentration at the edges is $C = X \times P$, the product of the solubility (X, mol m^{-3} Pa^{-1}) and partial pressure of H_2 (P, Pa). During the outgassing period, the concentration is zero. The model calculates the instantaneous rate of H_2 outgassing from the block as a function of time, diffusivity, and solubility ($G_{mod}(t,D,X)$, mol s^{-1}) by integrating the concentration of H_2 over the entire domain at each time step and dividing by the duration of the time step. The model does not account for adsorption of H_2 on the ice surface. Adsorption of H_2 on ice is negligible above 30 K (Kristensen et al., 2011) and sublimation from the ice surface would likely rapidly desorb any H_2 from the surface before the first injection into the GC/HePDD.

A fourth order Runge-Kutta integration scheme and a fixed time step of 1 s are used for the first 100 s of both the charging and outgassing periods when concentration gradients in the ice block are large. After 100 s, an adaptive Runge-Kutta-Fehlberg time stepping scheme is used to increase computational speed (Matthews & Fink, 2004). The time step increases to ~2,000 s by the end of each period when the concentration gradient is drastically reduced. A typical simulation for the conditions used in this study takes about 10 s, executing in MATLAB on an Intel Core-i7 processor running Windows 10. The model iterates over many combinations of solubility and diffusivity to optimize the fit of the modeled rate of outgassing to the measured rate of outgassing. We calculate the rate of H_2 outgassing from the ice ($G(t)$, mol s^{-1}) based on the measured mole fraction on the downstream side:

$$G(t) = H_2(t) * \frac{P_{air} F_{air}}{RT} \tag{2}$$

where $H_2(t)$ is the time variant measured mole fraction, P_{air} is the air pressure in the outgassing cell (1 atm), F_{air} is the volumetric flow of air through the sample loop, T is the temperature of the sample loop, and R is the ideal gas constant.

2.2.1. Analysis of H_2 in Air

H_2 was analyzed in the air streams from the diffusion cells using gas chromatography with pulsed-discharge helium photoionization detection (GC- Agilent 7890A; Valco Instruments D-3-I-7890 HePDD; Novelli et al., 2009). The air stream was directed through a stainless steel sample loop (3 mL loop of coiled 1/8" stainless steel tubing) and vented to the atmosphere. The loop was periodically (12-min intervals) injected into the He carrier gas stream of the gas chromatograph. Chromatographic separation was carried out on isothermal packed columns consisting of two HayeSep DB 100/120 mesh-packed stainless steel columns operated in series (Table 1). The first column was operated as a precolumn and switched out of the carrier flow 4 min after injection to prevent less volatile compounds from reaching the detector. A valve was mounted just before the detector to divert major components of air (O_2, N_2, Ar) from the detector as they eluted from the columns. The retention time for H_2 on the system is 3.7 min.

Table 1
Chromatographic Parameters for the GC-HePDD Analytical System

Parameter	Value
Carrier gas	99.999% pure He (Airgas Inc.)
Precolumn	5 m × 1/8 in. OD HayeSep DB 100/120 mesh
Analytical column	5 m × 1/8 in. OD HayeSep DB 100/120 mesh
Oven temperature	50°C
HePDD temperature	100°C
Column flow rate	35 mL min^{-1}
Discharge gas flow rate	3 mL min^{-1}

The system was calibrated using gas mixtures of 163–620 ppb H_2 in N_2 (ppb = nmol H_2/mol air) prepared in our laboratory in high pressure aluminum cylinders. The detector response is linear in H_2 ($R^2 = 0.99$). Under the conditions of these experiments (3 mL sample loop at atmospheric

pressure), reproducibility is estimated at 1.5% (1σ) and the limit of detection (2x the 1σ uncertainty in the intercept of the calibration curve) is estimated at 9 ppb.

3. Results

The raw data time series resulting from a block degassing experiment is shown in Figure 3a. H_2 levels in the air flow were initially ~1,000 ppb and declined with an initial rate of decrease of roughly 400 ppb h^{-1}. After 24 h, H_2 levels were on the order of 100 ppb and the rate of decrease had slowed to tens of ppb h^{-1}. The optimum diffusivity, solubility, and permeability (P) constants for each experiment were determined using the 3-dimensional diffusion model described earlier (Section 2.2). Optimization was carried out by running the model in forward mode using a grid of diffusivity and solubility values. Probabilities are assigned to each combination of diffusivity and solubility by assuming that the residuals between the modeled and measured H_2 levels are normally distributed with a variance equal to the analytical uncertainty:

$$Prob\left(D,X\right)=\frac{1}{\left(\sigma\sqrt{2\pi}\right)^{N}}e^{\frac{-1}{2\sigma^{2}}\sum_{t_0}^{t_N}\left(G_{mod}\left(t,D,X\right)-G\left(t\right)\right)^{2}} \quad (3)$$

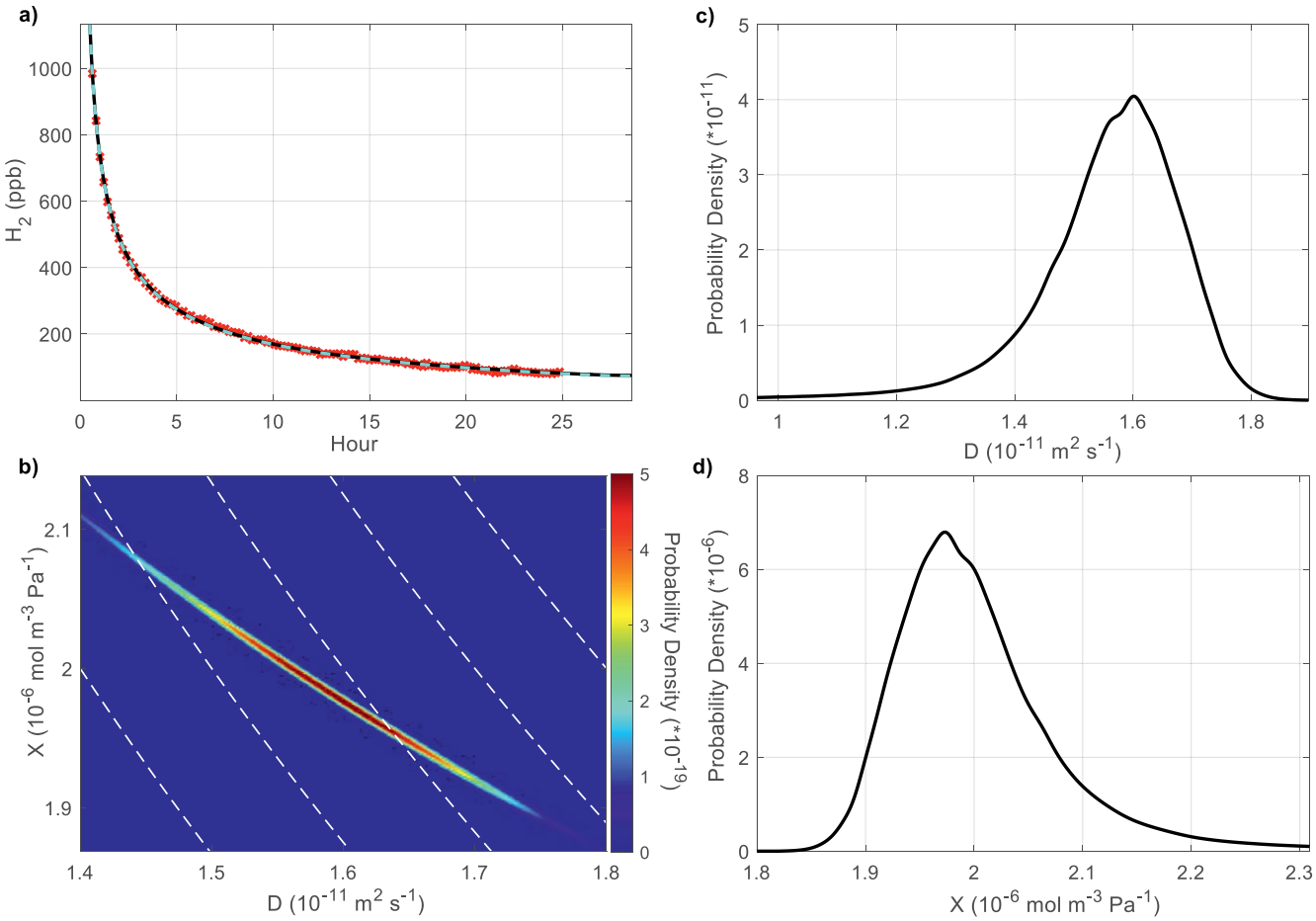

Figure 3. (a) Results from an experiment with Block A at 253 K with a charging time of 70.7 h. Red x's are measured H_2 mixing ratios. The dashed blue line is the expected mixing ratio from the numerical diffusion model using the optimal diffusivity and solubility constants (Table 2, row 1), and the black line is the expected mixing ratio using the Arrhenius fits in Table 3. The two lines are nearly identical. (b) Two dimensional probability distribution for diffusivity (D) and solubility (X) calculated for the same experiment. Dashed white lines are contours of constant permeability. (c) And (d) marginalized 1-dimensional probability distributions for D and X, respectively. The roughness of the marginalized probability distributions is non-physical and results from discretization. Note: The grid spacing used in (b), (c), and (d) is 1.0×10^{-3} for both diffusivity and solubility.

Table 2
Summary of Experimental Results for H_2 Diffusivity, Solubility, and Permeability Derived From the Individual Block Degassing Experiments

Ice block	Temperature (K)	Diffusivity (10^{-12} m^2 s^{-1})	Solubility (10^{-7} mol m^{-3} Pa^{-1})	Permeability (10^{-18} mol m^{-1} s^{-1} Pa^{-1})
A	252.7	$16.1^{+.7}_{-1.2}$	$19.6^{+.8}_{-.4}$	$31.8^{+.8}_{-1.3}$
	252.7	$13.2^{+3.4}_{-2.6}$	$17.3^{+2.6}_{-1.3}$	$25.1^{+2.8}_{-3.0}$
	227.2	$11.0^{+3.3}_{-2.8}$	$14.6^{+2.5}_{-1.4}$	$17.9^{+2.2}_{-2.4}$
	227.2	$10.2^{+4.3}_{-3.3}$	$15.1^{+3.5}_{-1.9}$	$18.2^{+3.2}_{-3.2}$
	204.2	$4.8^{+8.9}_{-2.5}$	$6.3^{+2.6}_{-.9}$	$10.7^{+1.0}_{-.3}$
	204.2	$22.7^{+3.7}_{-4.4}$	$7.2^{+1.0}_{-.5}$	$17.1^{+1.4}_{-1.7}$
	204.2	$17.1^{+4.9}_{-6.0}$	$7.4^{+1.6}_{-.7}$	$13.9^{+1.7}_{-2.4}$
	204.1	$10.5^{+8.2}_{-4.6}$	$8.3^{+3.3}_{-1.3}$	$13.2^{+3.0}_{-3.5}$
	203.2	$10.8^{+7.8}_{-4.9}$	$5.4^{+1.9}_{-.6}$	$10.4^{+1.2}_{-3.6}$
	199.2	$7.7^{+8.3}_{-3.7}$	$10.1^{+4.7}_{-1.7}$	$13.8^{+4.1}_{-3.5}$
B	252.7	$17.4^{+2.7}_{-2.2}$	$21.1^{+1.6}_{-1.4}$	$38.0^{+3.0}_{-2.6}$
	252.7	$11.1^{+1.5}_{-1.3}$	$22.6^{+1.7}_{-1.1}$	$25.7^{+1.6}_{-1.7}$
	227.2	$14.9^{+6.4}_{-4.4}$	$10.7^{+2.4}_{-1.3}$	$19.0^{+3.4}_{-3.1}$
	227.2	$12.6^{+5.1}_{-2.6}$	$13.1^{+2.0}_{-1.8}$	$18.4^{+3.4}_{-2.1}$
	204.2	$14.7^{+5.2}_{-6.5}$	$4.4^{+1.3}_{-.4}$	$7.9^{+.9}_{-2.2}$
	203.2	$9.0^{+11.1}_{-4.6}$	$5.8^{+2.6}_{-.9}$	$11.7^{+2.2}_{-4.2}$
	199.2	$13.1^{+9.2}_{-5.9}$	$5.0^{+1.9}_{-.6}$	$10.8^{+1.7}_{-3.4}$

Note. Uncertainties are ±1σ.

Table 3
Parameter Estimates for the Arrhenius Fits (A Factor and Energy of Activation, E_a) to the Diffusivity, Permeability, and Solubility of H_2

Parameter	A factor	E_a (J/mol)
Diffusivity (D)	$1.4^{+1.5}_{-.7}$*10^{-11} m^2 s^{-1}	-58^{+1450}_{-1450}
Solubility (X)	$1.3^{+.6}_{-.4}$*10^{-4} mol m^{-3} Pa^{-1}	8750^{+750}_{-730}
Permeability (P)	$1.9^{+1.1}_{-.6}$*10^{-15} mol m^{-1} Pa^{-1} s^{-1}	8660^{+840}_{-820}

Note. Uncertainties are ±1σ. The parameters were obtained using linear regression on the data in Figure 4.

where σ is the analytical uncertainty, and N is the number of samples in the run. The summation is performed over all sampling times. This process results in a two-dimensional probability distribution (Figure 3b). Permeation is well constrained by the block degassing experiments, with a relative uncertainty of roughly ±10% for the higher temperatures and ±30% at lower temperatures.

The fit between the model and the experiment allows the permeability to be partitioned into diffusivity and solubility. Marginalized probability distributions for diffusivity and solubility are obtained by integrating the two-dimensional probability distributions over the alternate dimension (Figures 3c and 3d). These are considerably broader than that for permeability because the inferred diffusivity and solubility from any given experiment are highly correlated (in a negative sense). For example, a low diffusivity constant paired with a high solubility constant can yield a similar modeled result to that from a high diffusivity constant paired with a low solubility constant. The relative 1σ uncertainties for diffusivity and solubility are roughly 30% at warmer temperatures and 50% at colder temperatures. These uncertainties are slightly skewed, resulting in asymmetrical uncertainties (Figure 3 and Table 2).

In total, 17 experiments were conducted using two different blocks of ice. These experiments were carried out at temperatures ranging from 199 to 253 K. The results are tabulated in Table 2 and plotted in Figure 4. Optimized diffusivity constants ranged from 4.8 to 22.7 × 10^{-12} m^2 s^{-1} and showed no temperature dependence. Optimized solubility constants ranged from 4.4 to 22.6 × 10^{-7} mol m^{-3} Pa^{-1}. The solubility data shows a strong temperature dependence. Optimized permeabilities ranged from 7.9 to 38.0 × 10^{-18} mol m^{-1} Pa^{-1} s^{-1}. The permeability data also shows strong temperature dependence reflecting the temperature dependence of solubility.

The diffusivity, solubility, and permeability data from the block degassing experiments were fit to an Arrhenius expression of the form:

$$k = A * e^{\frac{-E_a}{RT}} \quad (4)$$

where k is the constant of interest, A and E_a are the A factor and energy of activation. The Arrhenius fits and parameters are shown in Figure 4 and Table 3

4. Comparison to Prior Work

4.1. Diffusivity

To our knowledge, the only previous measurement of H_2 diffusivity in ice is Strauss et al. (1994) who inferred H_2 diffusivity in ice Ih from the energy distribution of scattered neutrons. They reported diffusion coefficients in the range of 10^{-9}–10^{-8} m^2 s^{-1} at temperatures between 25 and 60 K. Those results are two orders of magnitude larger than the results from the current study and comparable to the diffusivity of H_2 in liquid water (3–5 × 10^{-9} m^2 s^{-1}; Verhallen et al., 1984). Strauss et al. (1994) noted that these diffusivities were unexpectedly large and an order of magnitude larger than those of H atoms in the same study. The anomalously high diffusivity obtained from these neutron scattering experiments remains unexplained.

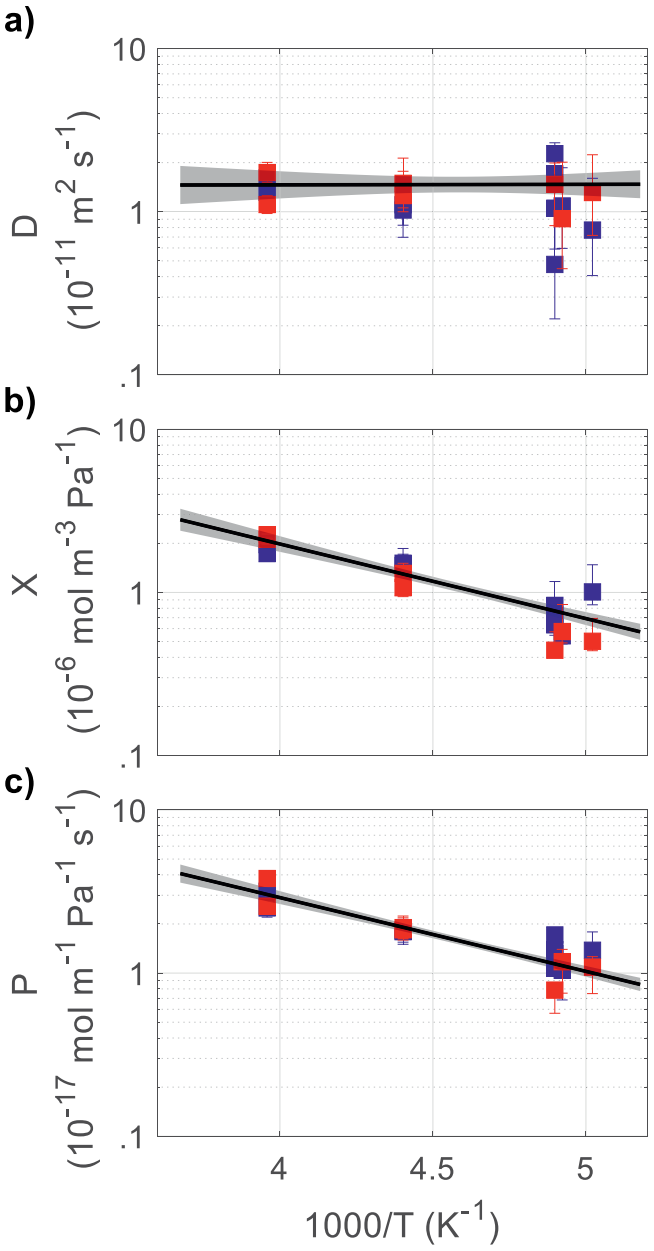

Figure 4. Optimized diffusivity (D), solubility (X), and permeability (P) constants obtained from the experiments. Error bars are ±1σ uncertainties. Blue squares correspond to ice Block A, and red squares correspond to Block B. Black lines are the Arrhenius fits with ±1σ uncertainty (Table 3).

Diffusivities have been published for some other small gases of atmospheric interest. Satoh et al. (1996) reported diffusion coefficients for He, Ne, and Ar using techniques similar to those used here. They report D_{He} and D_{Ne} values from 258 to 268 K that are greater than D_{H2} found in this study by factors of approximately 100 and 10, respectively (Figure 5a). Their D_{Ar} is slightly lower than D_{H2} by a factor of 2–3. Ikeda-Fukazawa et al. (2002, 2005) estimated D_{He}, D_{O2}, and D_{N2} based on molecular dynamics simulations. Our estimate of D_{H2} is substantially lower than their estimate for D_{He} at all temperatures. Their estimate for D_{O2} is similar to our result for D_{H2} at our lowest temperatures, but with a much stronger temperature dependence. At the high end of our temperatures (253 K), their D_{O2} is roughly a factor of 5 greater than D_{H2}. For N_2, diffusivity is lower than D_{H2} at low temperatures, and comparable to D_{H2} at the higher end.

4.2. Solubility

Ildyakov and Manakov (2014) reported the solubility of H_2 near the melting point (271–272 K) at pressures from 1.9–8 MPa. A linear fit through their data forced through the origin yields an H_2 solubility of 4.6×10^{-6} mol m^{-3} Pa^{-1}, in reasonable agreement with this study (Figure 5). Extrapolation of the Arrhenius fit to our data predicts a solubility of $2.8^{+.5}_{-.4} \times 10^{-6}$ mol m^{-3} Pa^{-1} at 272 K (Table 3). Two additional studies of H_2 solubility in ice reported data at pressures exceeding 40 MPa. We did not compare those high pressure measurements to our data because of the large extrapolation required.

The solubility of H_2 in ice is similar to that of He and substantially larger than those of Ne, O_2, and N_2. In terms of kinetic diameter (KD), He is smaller than H_2. O_2, Ar, and N_2 are larger. Ne is very similar in size to H_2. However, the diffusivity of H_2 is closer to that of O_2 than Ne and the solubility of H_2 is closer to that of He than Ne. KD is clearly not the only factor controlling these physical properties, and intermolecular forces must also be important.

The strong temperature dependence of H_2 solubility in ice is similar to the temperature dependence for the solubility of O_2 and N_2 predicted by the molecular dynamics simulations of Ikeda-Fukazawa et al. (2005). Interestingly, Ildyakov et al. (2013) reported a temperature dependence of the opposite sign for the solubility of He in ice. Investigating and explaining these inconsistencies will require further laboratory observations of the behavior of H_2 and other gases in ice.

5. Implications for Mobility of H_2 in Polar Firn Air and Ice

The permeability rates determined in this study can be used to examine how the mobility of H_2 influences the incorporation of atmospheric H_2 levels into the polar ice sheets and the behavior of H_2 in ice cores during recovery and storage.

5.1. Pore Close-Off Fractionation

Dissolution and diffusion of H_2 through the ice lattice can affect the composition of firn air and ice core bubbles. Pore close-off fractionation refers to the gradual pressurization of closed bubbles which drives a diffusive flux of gases between bubbles and open pores (Huber et al., 2006; Ikeda-Fukazawa et al., 2005;

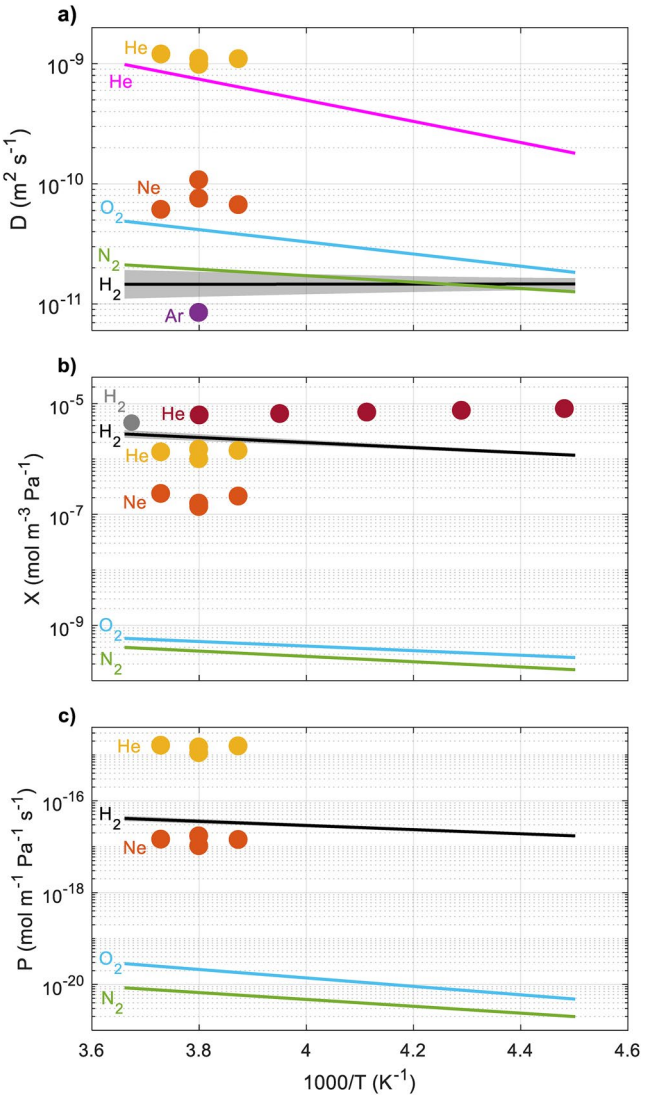

Figure 5. Comparison of (a) diffusivity, (b) solubility, and (c) permeability data from this study with literature data for H_2 and other gases. The plotted data is tabulated in Table 4. Filled circles: Gray - measured H_2 solubility (Ildyakov & Manakov, 2014); Yellow - measured diffusivity, solubility and permeation of He (Satoh et al., 1996); Orange - measured diffusivity, solubility and permeation of Ne (Satoh et al., 1996); Purple - measured Ar diffusivity (Satoh et al., 1996); maroon - measured solubility of He (Ildyakov et al., 2013). Lines: Black - Arrhenius fits to data from this study with ±1σ uncertainty (as in Figure 4); Magenta - estimated diffusivity of He from molecular dynamics simulations (Ikeda-Fukazawa et al., 2002); Blue and green lines-estimated diffusivity, solubility, and permeability of O_2 and N_2 from molecular dynamics simulations (Ikeda-Fukazawa et al., 2005).

Severinghaus & Battle, 2006). Significant enrichment of small, diffusive gases has been measured in the open pores at the base of the firn air lock-in zone where vertical gas phase diffusion within the open porosity is inhibited by impermeable winter layers. These impermeable layers allow much steeper concentration gradients to exist in the open porosity in the lock-in zone. Severinghaus & Battle (2006) reported that firn air samples from the base of the lock-in zone were enriched in ^{22}Ne by as much as 10%. Pore close-off fractionation begins well above the lock-in zone, leading to upward diffusion of the fractionated gas. As a result, ice core bubbles must be depleted in mobile gases such as Ne, relative to the overlying atmosphere.

Pore close-off fractionation must be accounted for when reconstructing past atmospheric levels of H_2 from firn air measurements using firn air models. At South Pole, neglecting this process leads to an overestimate of atmospheric levels of H_2 by ~10% during the early 1900s (Patterson et al., 2020). Pore close-off fractionation in firn air models has been parameterized in numerous ways. In Severinghaus and Battle (2006), small gases like Ne and H_2 diffuse through the thin walls of recently closed bubbles into the open porosity. The bubbles contribute to the fractionation until they have been compressed by 5% by firn densification. Beyond that point, bubbles cease to contribute to fractionation because they are assumed to be too far from open porosity. Patterson et al. (2020) refer to this model as the "kinetic model" because it implicitly assumes that diffusion through the ice lattice is a rate-limiting process. Alternatively, Patterson et al. (2020) proposed an "equilibrium model" of pore close-off fractionation in which H_2 diffusion through ice is sufficiently fast to equilibrate the partial pressure of H_2 between closed bubbles and open pores at the South Pole. Here we use the laboratory data from this study and a simple numerical diffusion model to examine the validity of the assumption of equilibrium.

The numerical model simulates radial diffusion from a single spherical, pressurized bubble through a concentric shell of ice into an outer shell of "open porosity" (Figure 6, inset). The closed bubble is assumed to have a volume of 10^{-10} m^3, corresponding to a radius of 0.288 mm. Equilibration time is calculated as a function of depth at the South Pole for depths where closed bubbles make up >1% of the total volume, beginning at a depth of 108 m. The porosity profile from the firn air model of Patterson et al. (2020) was used to prescribe the ice shell thickness and the volume of the "open porosity" shell. For each model run, the ratio of the volumes of the open porosity and closed bubble to total ice volume is identical to those ratios at the corresponding depth in the firn air model. The ice shell thickness decreases with depth from 1 mm at 108 m to 0.4 mm at 125 m because, in the firn air model, the ratio of ice volume to closed bubble volume decreases with depth. Likewise, open porosity volume decreases with depth from 1.0×10^{-9} m^3 at 108 m to 2.2×10^{-13} m^3 at 125 m because the ratio of open porosity volume to closed bubble volume in the firn air model decreases with depth. The model is initialized with H_2- free ice and equilibrium between the gas and ice is assumed at the boundaries of the bubble and the shell throughout the model run. The model calculation is carried out in one dimension, and non-radial diffusion is ignored. The diffusivity and solubility constants at the annual average temperature at South Pole (223 K) were calculated from the Arrhenius fits to the data from this study. The characteristic relaxation time (*e*-folding time) for equilibration is calculated and plotted in Figure 6. The characteristic relaxation time (τ) is defined as the time at which:

Table 4
Summary of the Diffusivity, Solubility, and Permeability Data From Various Literature Sources That is Plotted in Figure 5

Gas	Reference	Temp. K	Diffusivity D ($m^2\ s^{-1}$)	Solubility X (mol m^{-3} Pa^{-1})	Permeability P (mol m^{-1} Pa^{-1} s^{-1})
Discrete measurements:					
H_2	Ildyakov & Manakov, 2014	272	N/A	4.6×10^{-6}	N/A
He	Ildyakov et al., 2013	223	N/A	8.2×10^{-6}	N/A
		233	N/A	7.6×10^{-6}	N/A
		243	N/A	7.1×10^{-6}	N/A
		253	N/A	6.6×10^{-6}	N/A
		263	N/A	6.3×10^{-6}	N/A
He	Satoh et al., 1996	258	1.1×10^{-9}	1.4×10^{-6}	1.6×10^{-15}
		263	1.1×10^{-9}	1.0×10^{-6}	1.1×10^{-15}
		263	9.9×10^{-10}	1.5×10^{-6}	1.5×10^{-15}
		268	1.2×10^{-9}	1.4×10^{-6}	1.6×10^{-15}
Ne	Satoh et al., 1996	258	6.7×10^{-11}	2.1×10^{-7}	1.4×10^{-17}
		263	7.6×10^{-11}	1.4×10^{-7}	1.1×10^{-17}
		263	1.1×10^{-10}	1.6×10^{-7}	1.7×10^{-17}
		268	6.1×10^{-11}	2.4×10^{-7}	1.5×10^{-17}
Ar	Satoh et al., 1996	263	8.5×10^{-12}	N/A	N/A

		Diffusivity		Solubility		Permeability	
Arrhenius relationships:		A ($m^2\ s^{-1}$)	E_a (J mol^{-1})	A (mol m^{-3} Pa^{-1})	E_a (J mol^{-1})	A (mol m^{-1} Pa^{-1} s^{-1})	E_a (J mol^{-1})
H_2	This Work	1.4×10^{-11}	−58	1.3×10^{-4}	8,750	1.9×10^{-15}	8,660
He	Ikeda-Fukazawa et al., 2002	1.6×10^{-6}	16,830	N/A	N/A	N/A	N/A
O_2	Ikeda-Fukazawa et al., 2004	3.5×10^{-9}	9,700	1.9×10^{-8}	7,900	6.6×10^{-17}	17,600
N_2	Ikeda-Fukazawa et al., 2004	2.0×10^{-10}	5,100	2.3×10^{-8}	9,200	4.6×10^{-18}	14,400

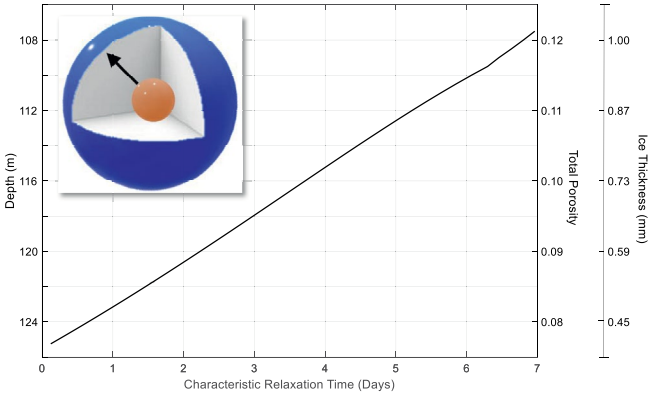

Figure 6. Results from a model simulation of H_2 diffusion between a pressurized bubble and unpressurized open pores showing characteristic relaxation time as a function of firn depth. Characteristic relaxation time is defined as the *e*-folding time for the equilibration of the partial pressure of H_2 in the outer shell of open porosity. Inset: An illustration of the geometry of the simulation. The bubble is at the center of an ice sphere with an outer "shell" of open porosity. H_2 diffuses from the inner bubble (orange) through the ice (white) to the outer "open porosity" (blue). Graph: Corresponding total porosity (i.e., open pore volume + closed bubble volume/firn volume) and model ice shell thickness for each depth is shown on the right *y*-axis.

$$\frac{P_{eq}}{P_{eq} - P_o(\tau)} = exp(1) \tag{5}$$

where P_{eq} is the equilibrium partial pressure of H_2 in the open porosity shell and P_o is the time-varying partial pressure of H_2 in the open porosity shell.

The *e*-folding time for the equilibration of the partial pressure of H_2 in the outer shell ranges from 7.0 days at 108 m to 0.1 day at 125 m. The rapid decrease in equilibration time with depth is driven by the decreasing ice shell thickness and by decreasing open pore volume. At South Pole, the annual accumulation rate is about 8 cm ice eq. y^{-1} and bubble pressurization in the firn column is roughly 0.1% y^{-1}. This model result suggests that the assumption of diffusive equilibrium between closed and open porosity is reasonable at the South Pole, and, given the short *e*-folding time, it is likely that the assumption of equilibrium is valid even at higher accumulation sites where bubble pressurization is more rapid. The geometry assumed in this calculation is highly oversimplified. In reality, the open pores are a complex web-like network, making it challenging to determine the average distance between closed bubbles and open pores (Burr et al., 2018, Figure 7). Images obtained from X-ray tomography of

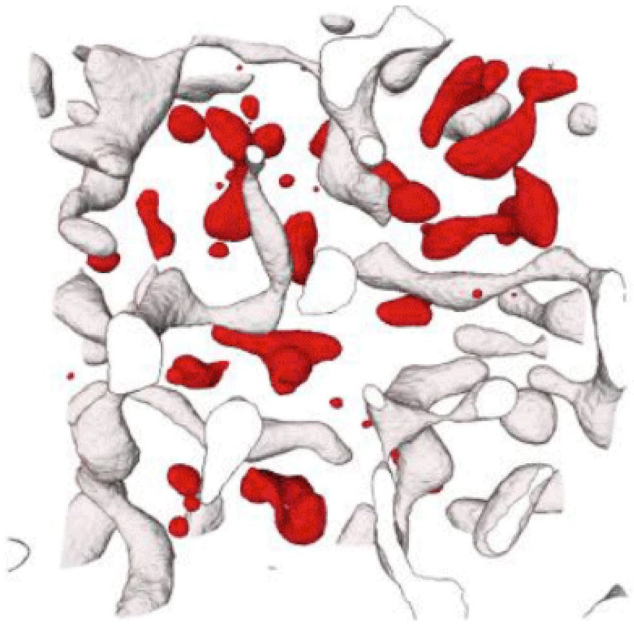

Figure 7. X-ray tomography image of the porosity field from just below the close-off depth (100 m) at Dome C. Below 100 m, firn air could not be sampled. Open pores are white and closed bubbles are red. The cross section is 6.72 × 6.72 mm. Reproduced with permission from Burr et al. (2018).

firn (Figure 7) could be used to develop more refined calculations of equilibration times for pore close-off fractionation.

5.2. Diffusive Migration of H_2 in the Ice Sheet

The internal pressure of air bubbles increases with depth below the firn/ice transition in response to the increasing hydrostatic pressure. The resulting increase in partial pressure of H_2 causes dissolution of H_2 from the bubble into the ice. This creates a vertical concentration gradient of H_2 in the ice and a net upward flux of H_2 in the ice sheet even in the case of constant atmospheric H_2 levels. The increase in H_2 partial pressure with depth likely continues until the bubble/clathrate transition is complete and no H_2 is present in the gas phase. This phenomenon has been observed previously with He (Craig & Chou, 1982; Jean-Baptiste et al., 1993, 2001)

To investigate the magnitude of this effect for H_2, we use a 1-dimensional finite difference advective/diffusive ice sheet model with layer thinning and ice densification (Neftel et al., 1983). The ice sheet model is discretized into annual layers. To isolate the effects of diffusion in the ice sheet from those associated with the firn layer (discussed in Section 5.1 above), the ice sheet model is not coupled to a firn air model. H_2 is assumed to be in equilibrium between ice and bubbles in each layer. The physical properties of South Pole were used for this calculation and a constant atmospheric mixing ratio was maintained. The model was run for 20,000 years and a steady state profile was achieved. The resulting vertical gradient was small (~1% m^{-1}). Upward diffusion was negligible, approximately 0.001% loss of H_2 from a single annual layer over 5,000 years. This result is consistent with the results of Jean-Baptiste et al. (1993), given that the permeability of H_2 is less than 0.01 times that of He.

We also investigated the diffusive smoothing of vertical gradients of H_2 in the ice sheet originating from fluctuations in atmospheric H_2 using the same model (Neftel et al., 1983). A 1-year pulse of H_2 is introduced at the surface and the model is run for 10,000 years. The amplitude of the resulting peak decreases, and the peak broadens due to vertical diffusion as it propagates through the ice sheet (Figure 8). The full width at half maximum (FWHM) for the 1-year pulse after propagating for 1,000 years is 0.6 m, which is equivalent to 10 years. After 10,000 years, the pulse FWHM is 4.5 m, equivalent to 78 years.

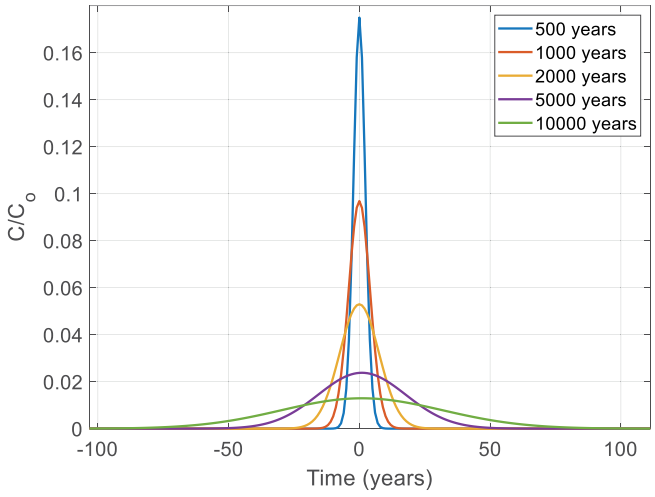

Figure 8. Model simulation of a pulse of H_2 propagating through the ice sheet at the South Pole. Length has been converted to time-scale on the *x*-axis.

Sites with higher annual accumulation experience a reduction in smoothing due to thicker annual layers. However, the effects of thicker layers are somewhat offset by the more rapid permeation associated with warmer temperatures. For example, under WAIS-Divide conditions (243 K, 22 cm ice eq. y^{-1}), the FWHM for a 1-year pulse is 6 years (0.8 m) after 1,000 years of propagation and 44 years (6.1 m) after 10,000 years of propagation. Annual layers are about 2.8 times thicker at WAIS-Divide than South Pole but smoothing is only attenuated by a factor of 1.7.

These results indicate that reconstructing high-frequency (decadal) atmospheric H_2 variability from polar ice cores will require some correction for diffusive smoothing. This could be accomplished by inverting an ice sheet model in a similar fashion to firn air reconstructions (e.g., Patterson et al., 2020; Petrenko et al., 2013). Smoothing of atmospheric variations also occurs due to gas phase diffusion in the firn column. At the South Pole, the age distribution of the H_2 incorporated into the ice sheet at the bottom of the firn column has a FWHM of ~13 years (Patterson et al., 2020). This smoothing in the firn air column is important to

account for with all ice core samples. In contrast, smoothing due to diffusion through the ice lattice is only important for samples that are more than several centuries old.

5.3. Post-Coring Diffusive Exchange With Atmospheric H_2

After an ice core has been drilled and brought to the surface, H_2 within the ice equilibrates with the surrounding atmosphere. The rate of this process dictates the procedures required to sample ice cores for analysis of paleoatmospheric H_2 levels. As described earlier, the hydrostatic compression of bubbles at depth drives H_2 from the bubbles into the ice. This effect causes newly drilled ice to be supersaturated with respect to atmospheric H_2. A similar phenomenon occurs for He, and post-coring diffusive losses for He have been estimated to be as much as 10% within 15 min of drilling and recovery (Jean-Baptiste et al., 1993, 2001). Haan (1996) reported measurements of H_2 in several stored ice cores, showing that the measured H_2 levels are roughly consistent with full equilibration with the ambient atmosphere in the storage freezer. However, the kinetics of diffusive exchange cannot be calculated from that data, as the storage time of the cores was not given.

Post-coring equilibration of H_2 was simulated using a finite difference model of diffusion in a uniform cylinder. The model assumes radial symmetry and a homogeneous distribution of bubbles. For this calculation we used the approximate properties of a 10 cm diameter South Pole ice core recovered from a depth of 200 m (223 K, accumulation rate 8 cm ice eq. y^{-1}). The bubble pressure was estimated from the ice sheet model described in section 5.2. The in-situ bubble pressure at 200 m is roughly 25 bar. H_2 in the bubbles at close-off was assumed to be 300 ppb, based on firn air measurements at the base of the lock-in zone at South Pole (Patterson et al., 2020). We make two simplifying assumptions in this calculation that both tend to overestimate the rate of diffusive equilibration. First, instantaneous equilibrium is assumed between the bubbles and the ice within each grid cell. Second, ice relaxation is neglected. Gow (1971) estimated a density change of 0.2%–0.3% over 16 months for a GISP2 ice core sample recovered from a depth of 200 m. This implies a 7%–10% decrease in bubble pressure over that time span. Therefore, this calculation serves as an upper bound on diffusive losses of H_2 from a bubbly ice core. Diffusion and solubility coefficients were obtained using the Arrhenius parameters in Table 3 for 253 K, a typical storage freezer temperature.

The model simulation is run for one year of sample storage at ambient atmospheric levels of 530 ppb H_2. The results show that over one year, the ice core sample loses only 18% of its H_2 (ure 9). This calculation suggests that bubbly ice core samples could still be meaningfully analyzed for H_2 after storage for several months in the ambient atmosphere provided that the outermost ice is removed before extraction. A caveat to this conclusion is the possible additional loss of H_2 via microfractures associated with drilling and ice relaxation. Small losses of Ar and O_2 (1%–2%) have been observed during storage and attributed to microfractures in the ice lattice associated with drilling and extraction (Bender et al., 1995). These losses ceased after 3 months presumably because of microfracture healing. It is possible that microfracture-related losses of H_2 could be greater due to its smaller molecular diameter, but the size dependence of this phenomenon has not been established.

We also considered the case of deep ice core samples in which some or all of the enclosed air is bound in clathrate hydrates. Air bubbles transform into air clathrate inclusions in the ice lattice at depths between 500 and 1,700 m, depending on site temperature and accumulation rate, (Miller, 1969; Salamatin et al., 1998; Shoji & Langway, 1982). Pure H_2 clathrates do not form in polar ice sheets because the dissociation pressure of such clathrates ($\sim 10^9$ Pa at 223 K) is substantially higher than *in situ* pressures (Mao & Mao, 2004; Vos et al., 1993). Experimental evidence shows that H_2 can occupy various sites in N_2 clathrates as a guest molecule. Lu et al. (2012) exposed N_2 clathrates to pure H_2 at 150 bar and observed formation of mixed clathrates with between 1 and 3 H_2 molecules per N_2 molecule. Those results are not directly transferable to clathrates in an ice sheet where N_2 is $\sim 10^7$ times more abundant than H_2. Instead, we estimated the fractional occupancy of clathrates in polar ice using Kihara potentials after Mousis et al. (2013) and Parrish and Prausnitz (1972). Using this approach, we calculated the partitioning of H_2 between the dissolved phase, the gas phase, and clathrates (both large and small cage) occupied by a mixture of N_2, O_2, Ar, and H_2. These are thermodynamic calculations that do not account for the kinetics of clathrate nucleation and growth or for the non-hydrostatic behavior of bubbles (Salamatin et al., 1998). This calculation also requires some air to remain in the gas phase (bubbles) at all pressures. In actuality, bubbles are no longer observed below the bubble/clathrate transition

Table 5
Comparison of Gas Partitioning for a System With Only Bubbles and for a System With Bubbles in Thermodynamic Equilibrium With Clathrates

		Bubble (mole fraction)				Clathrate (mole fraction)				Ice (mol m^{-3})
Condition	Pressure P (Pa)	N_2	O_2	Ar	H_2	N_2	O_2	Ar	H_2	H_2
Bubbles only	7.6×10^9	0.78	0.21	0.010	1.8×10^{-10}	N/A	N/A	N/A	N/A	1.6×10^{-6}
Bubbles and clathrates	3.8×10^6	0.90	0.098	2.3×10^{-3}	3.5×10^{-7}	0.78	0.21	0.01	1.2×10^{-8}	1.6×10^{-6}

depth (e.g., below 1,300 m at South Pole; Ackermann et al., 2006). These simplifications notwithstanding, the calculation should estimate the impact of clathrate formation on H_2 mobility in deep polar ice.

Parameters for the calculations include Kihara potential parameters for N_2, O_2, Ar, and H_2 (Khan et al., 2015; Mousis et al., 2013) and Structure II clathrate physical parameters from Mousis et al. (2013). Dissociation pressures for pure clathrates of N_2, O_2, Ar at 223 K were calculated after Mousis et al. (2013). The dissociation pressure of pure H_2 clathrates was estimated from an Arrhenius fit to the data in Mao and Mao (2004).

The following case is an example illustrating how clathrates influence the behavior of H_2 in ice. We use conditions similar to those at the base of the bubble-clathrate transition zone at South Pole: (a) A bubble volume to ice volume ratio of 10^{-6}, (b) a total gas pressure of 7.6×10^9 Pa if no clathrates were present, (c) total gas composition of 0.78 N_2, 0.21 O_2, 0.01 Ar, and 400 ppb H_2 (including H_2 in both the dissolved and gas phases). The amount of N_2, O_2, and Ar dissolved in the ice lattice is negligible compared to the clathrate and gas phase, and is ignored in these calculations. At equilibrium under these conditions, 99.95% of the total gas present in the system is enclathrated and 0.05% of the total gas present in the system remains in the gas phase at a pressure of 3.8×10^6 Pa. 97.0% of the H_2 present in the system is dissolved in the ice lattice, 3.0% partitions into the clathrates, and 0.04% remains in the gas phase (Table 5). The small amount of H_2 present in the clathrate phase reflects the small magnitude of the Kihara potential well of an enclathrated H_2 molecule.

Diffusive losses of H_2 from a bubble-free clathrate ice sample with these characteristics were calculated using the Crank (1975) solution for radial diffusion in a cylinder. To facilitate the calculation, we make two simplifying assumptions: (a) All of the H_2 is dissolved in the ice lattice (rather than the ~97% predicted from

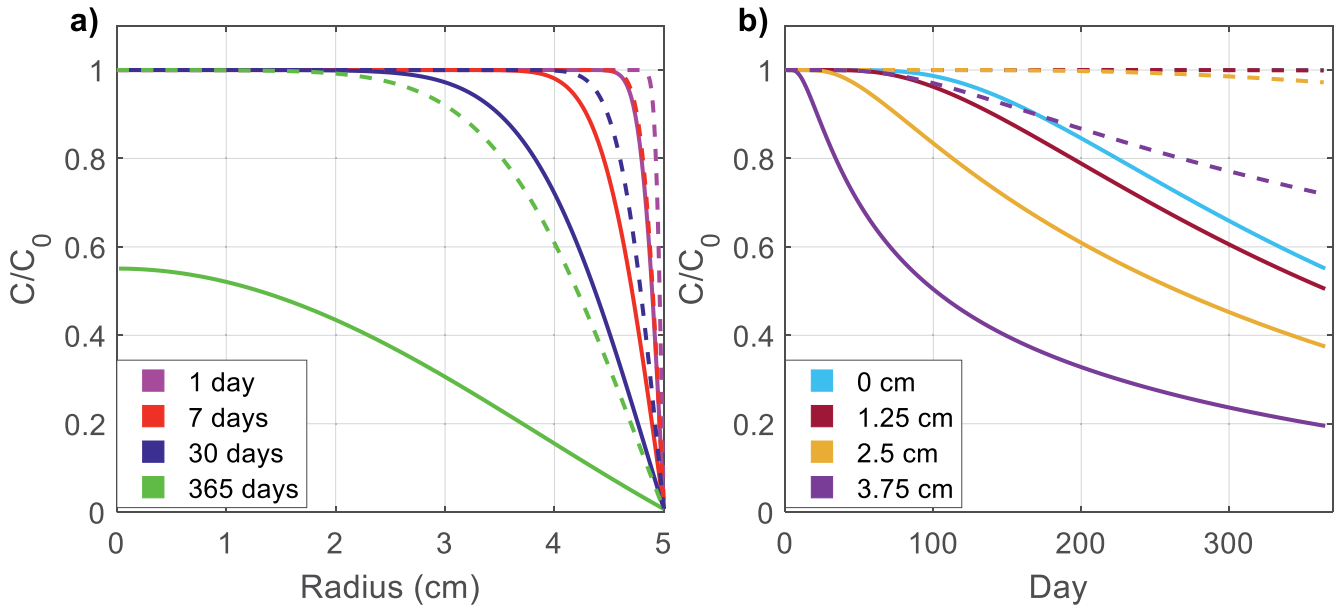

Figure 9. Model simulation of equilibration of ice core samples recovered from South Pole for bubbly and bubble-free clathrate ice. The fraction of initial H_2 remaining is plotted as a function of distance from the center of a 10 cm diameter ice core and of storage time after drilling. Dashed lines: Bubble-containing (200 m) ice, Solid lines: Bubble-free clathrate ice. (a) Curves show the profile after 1 day (magenta), 7 days (red), 30 days (blue), and 365 days (green). (b) Curves show the time course at radii of 0 cm (light blue), 1.25 cm (maroon), 2.5 cm (yellow), and 3.75 cm (purple).

the Kihara calculation), and (b) as before, ice relaxation during storage is ignored, although Gow (1971) estimated that the volume of a GISP2 sample recovered from 1,000 m increased by 0.3%–0.4% over 16 months. The results show that after 1 year, the bubble free ice has lost 66% of the H_2 initially present in the sample (Figure 9). This simulation provides an upper limit on diffusive losses of H_2 from clathrate ice. H_2 concentrations in clathrate ice are much higher than in bubbly ice because H_2 partitions almost exclusively into the dissolved phase in clathrate ice. The greater supersaturation in H_2 relative to the atmosphere causes faster diffusive losses from clathrate ice upon sample recovery. As a result, it is evident that ice core samples containing clathrates intended for analysis of H_2 should be enclosed in an impermeable container after drilling to prevent diffusive exchange with the modern atmosphere.

6. Conclusions

The permeability of H_2 in ice was experimentally measured at temperatures relevant to polar ice and partitioned into diffusivity and solubility constants. H_2 permeability in ice exhibits positive temperature-dependence. The temperature dependence of permeation appears to be fully explained by that of solubility while diffusivity appears to be temperature invariant. This is a surprising result because conceptual models for diffusion of gases in ice typically invoke an activation energy associated with the mobility of vacancies in the lattice or potential fields between the ice and diffusing gas molecules (Ikeda-Fukazawa et al., 2002, 2004, 2005). There is little experimental data in the literature with which to validate this finding. Satoh et al. (1996) reported temperature-independent diffusivity of Ne in ice, but that study covered only a 10 K temperature range. If temperature independence of diffusivity proves correct, it would suggest that the mechanism of diffusion is more complex than previously assumed. Further experimental work on the diffusion of small gases in ice is warranted and the experimental methodology developed here is easily extended to other gases.

The permeability of H_2 allows estimation of the rates of processes relevant to reconstructing the atmospheric history of H_2 from polar firn air and ice cores. H_2 permeation is likely to result in equilibration between open and closed pores in the firn column. Such equilibration simplifies firn air modeling for H_2 (Patterson et al., 2020). H_2 permeation in polar ice leads to diffusive smoothing of vertical gradients. For ice with gas ages of several centuries, this smoothing is comparable to that caused by diffusion during firn air enclosure. Finally, we estimate the rate of exchange of ice core samples with the atmosphere and find that the permeation of H_2 from bubbly ice should be slow enough to permit analysis of H_2 up to a year after drilling (barring additional losses via microfractures).

Data Availability Statement

The data used for this work are available at the DRYAD data repository (https://datadryad.org/; https://doi.org/10.7280/D1F973).

Acknowledgments
The authors wish to thank Cyril McCormick and Armando Vilchez for their work in building the temperature control system. This manuscript benefitted greatly from the comments of two anonymous reviewers. This research was supported by the NSF Antarctic Glaciology program (OPP-1907974).

References

Ackermann, M., Ahrens, J., Bai, X., Bartelt, M., Barwick, S. W., Bay, R. C., et al. (2006). Optical properties of deep glacial ice at the South Pole. *Journal of Geophysical Research*, *111*(13), 1–26. https://doi.org/10.1029/2005JD006687

Ahn, J., Headly, M., Brook, E. J., Wahlen, M., Mayewski, P. A., & Taylor, K. C. (2008). CO_2 diffusion in polar ice: Observations from Naturally formed CO_2 spikes in the Siple Dome (Antarctica) ice core. *Journal of Glaciology*, *54*(187), 685–695. https://doi.org/10.3189/002214308786570764

Bender, M., Sowers, T., & Lipenkov, V. (1995). On the concentrations of O_2, N_2, and Ar in trapped gases from ice cores. *Journal of Geophysical Research*, *100*(D9), 18651–18660. https://doi.org/10.1029/94jd02212

Bereiter, B., Schwander, J., Lüthi, D., & Stocker, T. F. (2009). Change in CO_2 concentration and O_2/N_2 ratio in ice cores due to molecular diffusion. *Geophysical Research Letters*, *36*(5), 1–5. https://doi.org/10.1029/2008GL036737

Burr, A., Ballot, C., Lhuissier, P., Martinerie, P., Martin, C. L., & Philip, A. (2018). Pore morphology of polar firn around closure revealed by X-ray tomography. *The Cryosphere*, *12*(7), 2481–2500. https://doi.org/10.5194/tc-12-2481-2018

Craig, H., & Chou, C. C. (1982). Helium isotopes and gases in Dye 3 ice cores. *Eos*, *63*, 298.

Crank, J. (1975). *The Mathematics of Diffusion* (Vol. 2, pp. 269–103). Oxford, UK: Clarendon Press.

Etheridge, D. M., Steele, L. P., Francey, R. J., & Langenfelds, R. L. (1998). Atmospheric methane between 1000 A.D. and present: Evidence of anthropogenic emissions and climatic variability. *Journal of Geophysical Research*, *103*(D13), 15979–15993. https://doi.org/10.1029/98jd00923

Etheridge, D. M., Steele, L. P., Langenfelds, R. L., Francey, R. J., Barnola, J.-M., & Morgan, V. I. (1996). Natural and anthropogenic changes in atmospheric CO_2 over the last 1000 years from air in Antarctic ice and firn. *Journal of Geophysical Research*, *101*(D2), 4115–4128. https://doi.org/10.1074/jbc.271.44.2750910.1029/95jd03410

Gow, A. J. (1971). Relaxation of ice in deep drill cores from Antarctica. *Journal of Geophysical Research*, *76*(11), 2533–2541. https://doi.org/10.1029/jb076i011p02533

Haan, D. (1996). *Teneurs en monoxyde de carbone de l ' air contenu dans la glace de l ' Antarctique et du Groenland*. Universite Joseph Fourier- Grenoble 1.

Huber, C., Beyerle, U., Leuenberger, M., Schwander, J., Kipfer, R., Spahni, R., et al. (2006). Evidence for molecular size dependent gas fractionation in firn air derived from noble gases, oxygen, and nitrogen measurements. *Earth and Planetary Science Letters*, *243*, 61–73. https://doi.org/10.1016/j.epsl.2005.12.036

Ikeda-Fukazawa, T., Fukumizu, K., Kawamura, K., Aoki, S., Nakazawa, T., & Hondoh, T. (2005). Effects of molecular diffusion on trapped gas composition in polar ice cores. *Earth and Planetary Science Letters*, *229*(3–4), 183–192. https://doi.org/10.1016/j.epsl.2004.11.011

Ikeda-Fukazawa, T., Horikawa, S., Hondoh, T., & Kawamura, K. (2002). Molecular dynamics studies of molecular diffusion in ice Ih. *The Journal of Chemical Physics*, *117*(8), 3886–3896. https://doi.org/10.1063/1.1495844

Ikeda-Fukazawa, T., Kawamura, K., & Hondoh, T. (2004). Mechanism of molecular diffusion in ice crystals. *Molecular Simulation*, *30*(13–15), 973–979. https://doi.org/10.1080/08927020410001709307

Ildyakov, A. V., & Manakov, A. Y. (2014). Solubility of hydrogen in ice Ih at pressures up to 8 MPa. *International Journal of Hydrogen Energy*, *39*, 18958–18961. https://doi.org/10.1016/j.ijhydene.2014.09.069

Ildyakov, A. V., Manakov, A. Y., Aladko, E. Y., Kosyakov, V. I., & Shestakov, V. A. (2013). Solubility of helium in ice Ih at pressures up to 2000 bar: Experiment and calculations. *Journal of Physical Chemistry B*, *117*(25), 7756–7762. https://doi.org/10.1021/jp400985w

Jean-Baptiste, P., Petit, J.-R., Lipenkov, V. Y., Raynaud, D., & Barkov, N. I. (2001). Constraints on hydrothermal processes and water exchange in Lake Vostok from helium isotopes. *Nature*, *411*, 460–462. https://doi.org/10.1038/35078045

Jean-Baptiste, P., Raynaud, D., Mantisi, F., Sowers, T., & Barkov, N. (1993). Measurement of helium isotopes in Antarctic ice: Preliminary results from Vostok. *Comptes rendus de l'Académie des Sciences*, *316*(2), 491–497.

Khan, M. N., Rovetto, L. J., Peters, C. J., Sloan, E. D., Sum, A. K., & Koh, C. A. (2015). Effect of hydrogen-to-methane concentration ratio on the phase equilibria of quaternary hydrate systems. *Journal of Chemical & Engineering Data*, *60*(2), 418–423. https://doi.org/10.1021/je500675q

Kristensen, L. E., Amiaud, L., Fillion, J.-H., Dulieu, F., & Lemaire, J.-L. (2011). H_2, HD, and D_2 abundances on ice-covered dust grains in dark clouds. *Astronomy & Astrophysics*, *44*, 1–7. https://doi.org/10.1051/0004-6361/200912124

Lu, H., Wang, J., Liu, C., Ratcliffe, C. I., Becker, U., Kumar, R., & Ripmeester, J. (2012). Multiple H_2 occupancy of cages of clathrate hydrate under mild conditions. *Journal of the American Chemical Society*, *134*(22), 9160–9162. https://doi.org/10.1021/ja303222u

Lüthi, D., Bereiter, B., Stauffer, B., Winkler, R., Schwander, J., Kindler, P., et al. (2010). CO_2 and O_2/N_2 variations in and just below the bubble-clathrate transformation zone of Antarctic ice cores. *Earth and Planetary Science Letters*, *297*(1–2), 226–233. https://doi.org/10.1016/j.epsl.2010.06.023

Manakov, A. Y., Aladko, E. Y., & Ildyakov, A. V. (2017). Solubility of hydrogen in ice Ih along the ice melting curve. *International Journal of Hydrogen Energy*, *42*(1), 322–326. https://doi.org/10.1016/j.ijhydene.2016.12.120

Mao, W. L., & Mao, H. K. (2004). Hydrogen storage in molecular compounds. *Proceedings of the National Academy of Sciences of the United States of America*, *101*(3), 708–710. https://doi.org/10.1073/pnas.0307449100

Matthews, J. H., & Fink, K. K. (2004). *Numerical methods using MATLAB* (4th ed.). Prentice-Hall.

Miller, S. L. (1969). Clathrate hydrates of air in Antarctic ice. *Science*, *165*(3892), 489–490. https://doi.org/10.1126/science.165.3892.489

Mousis, O., Chassefière, E., Lasue, J., Chevrier, V., Elwood Madden, M. E., Lakhlifi, A., et al. (2013). Volatile trapping in martian clathrates. *Space Science Reviews*, *174*(1–4), 213–250. https://doi.org/10.1007/s11214-012-9942-9

Namiot, A. Y., & Gorodetskaya, L. Y. Solubility of gases in ice solubility of gases in ice. *Proceedings of the USSR Academy of Sciences*, 190(3), 604–605.

Neftel, A., Oeschger, H., Schwander, J., & Stauffer, B. (1983). Carbon dioxide concentration in bubbles of natural cold ice. *Journal of Physical Chemistry*, *87*(21), 4116–4120. https://doi.org/10.1021/j100244a025

Noguchi, M., Tachibana, S., & Nagahara, H. (2019). Diffusivity and solubility of methane in ice Ih. *Geochemical Journal*, *53*(1), 83–89. https://doi.org/10.2343/geochemj.2.0537

Novelli, P. C., Crotwell, A. M., & Hall, B. D. (2009). Application of gas chromatography with a pulsed discharge helium ionization detector for measurements of molecular hydrogen in the atmosphere. *Environmental Science & Technology*, *43*, 2431–2436. https://doi.org/10.1021/es803180g

Novelli, P. C., Lang, P. M., Masarie, K. A., Hurst, D. F., Myers, R., & Elkins, J. W. (1999). Molecular hydrogen in the troposphere: Global distribution and budget. *Journal of Geophysical Research*, *104*(D23), 30427–30444. https://doi.org/10.1029/1999jd900788

Parrish, W. R., & Prausnitz, J. M. (1972). Dissociation pressures of gas hydrates formed by gas mixtures. *Industrial & Engineering Chemistry Product Research and Development*, *11*(1), 26–35. https://doi.org/10.1021/i260041a006

Patterson, J. D., Aydin, M., Crotwell, A. M., Petron, G., Severinghaus, J. P., & Saltzman, E. S. (2020). Atmospheric history of H_2 over the past century reconstructed from South Pole firn air. *Geophysical Research Letters*, *47*(14), 1–8. https://doi.org/10.1029/2020GL087787

Petrenko, V. V., Martinerie, P., Novelli, P., Etheridge, D. M., Levin, I., Wang, Z., et al. (2013). A 60 yr record of atmospheric carbon monoxide reconstructed from Greenland firn air. *Atmospheric Chemistry and Physics*, *13*(15), 7567–7585. https://doi.org/10.5194/acp-13-7567-2013

Salamatin, A. N., Hondoh, T., Uchida, T., & Lipenkov, V. Y. (1998). Post-nucleation conversion of an air bubble to clathrate air-hydrate crystal in ice. *Journal of Crystal Growth*, *193*(1–2), 197–218. https://doi.org/10.1016/S0022-0248(98)00488-6

Satoh, K., Uchida, T., Hondoh, T., & Mae, S. (1996). Diffusion coefficient and solubility measurements of noble gases in ice crystals. *Proceedings of the NIPR Symposium on Polar Meteorology and Glaciology*, *10*, 73–81.

Severinghaus, J., & Battle, M. (2006). Fractionation of gases in polar ice during bubble close-off: New constraints from firn air Ne, Kr and Xe observations. *Earth and Planetary Science Letters*, *244*, 474–500. https://doi.org/10.1016/j.epsl.2006.01.032

Shoji, H., & Langway, C. C. (1982). Air hydrate inclusions in fresh ice core. *Nature*, *298*(5874), 548–550. https://doi.org/10.1038/298548a0

Strauss, H. L., Chen, Z., & Loong, C. K. (1994). The diffusion of H_2 in hexagonal ice at low temperatures. *The Journal of Chemical Physics*, *101*(8), 7177–7180. https://doi.org/10.1063/1.468303

Verhallen, P. T. H. M., Oomen, L. J. P., Elsen, A. J. J. M. v. d., Kruger, J., & Fortuin, J. M. H. (1984). The diffusion coefficients of helium, hydrogen, oxygen and nitrogen in water determined from the permeability of a stagnant liquid layer in the quasi-steady state. *Chemical Engineering Science*, *39*(11), 1535–1541. https://doi.org/10.1016/0009-2509(84)80082-2

Vos, W. L., Finger, L. W., Hemley, R. J., & Mao, H. K. (1993). Novel H_2-H_2O clathrates at high pressures. *Physical Review Letters*, *71*(19), 3150–3153. https://doi.org/10.1103/PhysRevLett.71.3150